Volume Reconstruction of Cone-Beam Geometry

Tsutomu Gomi[*]

School of Allied Health Sciences, Kitasato University, 1-15-1 Kitasato, Sagamihara, Kanagawa, 228-8555, Japan

Abstract: The purpose of this manuscript is to provide a tutorial overview on the subject of cone-beam geometry devices imaging. Toward this end, we have tried to strike a balance among purely algorithmic issues, topics (tomosynthesis imaging etc.) dealing with how to generate data for reconstruction in different domains, and artifacts inherent to different data collection strategies.

This manuscript is structured to cover the basics of reconstruction from x-ray modern cone-beam geometry. Some results from simulations and real measurements are presented in order to give an explanation of the various pitfalls of the most used reconstruction techniques. However, the main focus of the paper is concerned with detailed derivations of reconstruction algorithms in modern cone-beam CT (CBCT) and digital tomosynthesis systems. A thorough analysis of artifacts and a discussion of practical issues, such as dose considerations, provide further insight into modern cone-beam geometry systems. We hope that the optimal volumetric reconstruction system which it can cone-beam geometry in high quality and a low radiation exposure dose in the near future.

Keywords: Cone-beam CT, tomosynthesis, reconstruction algorithm, 3D imaging.

1. INTRODUCTION

For cone-beam computed tomography (CT) scanning systems, volume reconstruction algorithms have been developed and applied in various studies in order to show their potential for use in future applications. As is true for standard medical CT systems with one-dimensional detectors, because the basic system geometry is unchanged for cone-beam CT scanners, two different scanning modes are of particular interest: circular and helical modes. These are of special interest for applications such as medical imaging and nondestructive testing. The problem of cone-beam reconstruction for helical source-detector trajectories is a topic of ongoing discussion [1-9, 37, 38]. The method developed by Feldkamp *et al.* [10] seems to be the most used technique for circular trajectories.

Apart from its easy implementation, it is exact for scanning objects in the central plane containing the circular source trajectory and those that are homogeneous in the direction parallel to the rotation axis. Since the method was reported, it has been used most widely for three-dimensional (3D) cone-beam reconstruction. The inexactness of the Feldkamp algorithm is a consequence of the missing data problem. The 3D Radon transform cannot be determined completely when projection data are acquired along a circular source-detector trajectory [11, 12]. Nevertheless, circular trajectories may be used in future cone-beam CT systems because artifacts are produced in Radon space due to missing small cone angles.

In the biomedical field, the most popular method for cone-beam image reconstruction is the 3D filtered back-projection (FBP), which uses a circular scanning locus and reconstructs images well in case of a small cone angle [10]. However, the Feldkamp algorithm produces significant image artifacts, such as decrease of intensity from the mid-plane, in case of a moderate to large cone angle. Consequently, several variants of the Feldkamp algorithm were developed for practical applications that involve larger cone angles [13-20].

Interest in tomosynthesis and its clinical applications has been revived by recent advances in digital X-ray detector technology. Conventional tomography technology provides planar information of an object from its projection images. In tomography, an X-ray tube and an X-ray film receptor are positioned on either side of the object. The relative motion of the tube and film is predetermined based on the location of the in-focus plane [21]. A single image plane is generated by a scan, and multislice CT scans are required to provide a sufficient number of planes to cover the selected structure in the object. Tomosynthesis acquires only one set of discrete X-ray projections that can be used to reconstruct any plane of the object retrospectively [22]. The technique has been investigated in angiography and imaging of the chest, hand joints, lungs, teeth, and breasts [23-28]. A review of tomosynthesis has been given by Dobbins *et al.* [29]. Tomosynthesis was shown to outperform planar imaging to a statistically significant extent. Various types of tomosynthesis reconstruction methods have been explored.

2. CURRENT STATUS AND PROBLEM

CT (including cone-beam CT) provides images of bony components have the higher signal in CT images. However, this can be sufficient for the final diagnosis in a number of pathological conditions. Pathological changes, such as

*Address correspondence to this author at the School of Allied Health Sciences, Kitasato University, Graduate School of Medicine, Kitasato University, 1-15-1 Kitasato, Sagamihara, Kanagawa, 228-8555, Japan; Tel: +81(0) 427789617; Fax: +81(0)427789628; E-mail: gomi@kitasato-u.ac.jp

formation of osteophytes, erosion, fractures, ankylosis, and developmental abnormalities, as well as the position of the condyle in the fossa, can be detected on CT images. The main disadvantage of CT examination (especially in cases in which multislice CT is used) remains the requirement of high radiation doses.

Since the discovery of X-rays in 1895 and their application to dentistry, radiographic imaging of oral anatomy has consisted primarily of viewing 3D structures projected onto a two-dimensional (2D) plane. This form of imaging, known as radiography, is characterized by a point source of radiation producing a beam that passes through the patient and strikes a relatively flat image receptor (usually a film). This essentially produces an attenuation map of the structures through which the beam has been transmitted. While the dental profession has relied on this method for obtaining information about the hard tissues of the oral cavity, it inevitably superimposes anatomy and metallic restorations, which confounds the problem of identifying and/or localizing diseases or objects in three dimensions.

Recently, medical CT began a transition from fan-beam to cone-beam geometry with the introduction of multislice CT systems [6-8]. These systems allow scanning of regions requiring a broad scanning range, such as the chest and abdomen, because they use a multislice CT employing a large number of channels (i.e., 128 and 256 rows etc). Use of a wide-range cone-beam CT with a wide angle results in reconstructions with low image quality accompanied by

cone-beam artifacts in the reconstruction planes away from the mid-plane in the longitudinal direction. A cone-beam CT with a wide angle, which reduces cone-beam artifacts and generates high-quality reconstruction images with a wide exposure range, would thus be clinically very useful.

Therefore, this method has been adopted for image reconstruction of 3D tomography and multidetector cone-beam CT. A number of improved 3D reconstruction methods have been derived from the Feldkamp method. However, increases in artifacts are generally separated from the central plane to the far direction. Here, we focus on the potential application of digital tomosynthesis (linear motion) using an amorphous selenium flat-panel detector in which a modified 3D FBP reconstruction algorithm is used for improving the performance in imaging the temporomandibular joint and chest phantom.

3.   THREE-DIMENSIONAL   RECONSTRUCTION ALGORITHM

3.1. Cone-Beam CT System

3.1.1. Feldkamp Algorithm

By analogy to 2D FBP, the cone-beam data were acquired along a circular source-detector trajectory (Fig. **1**). Figure **2** shows the simulation results obtained by the 2D and 3D FBP methods for an object having 3D information (the Shepp-Logan 3D phantom was used). The 2D FBP method was not reproducible and it was difficult to regard a geometric variation of an image, but the 3D FBP method
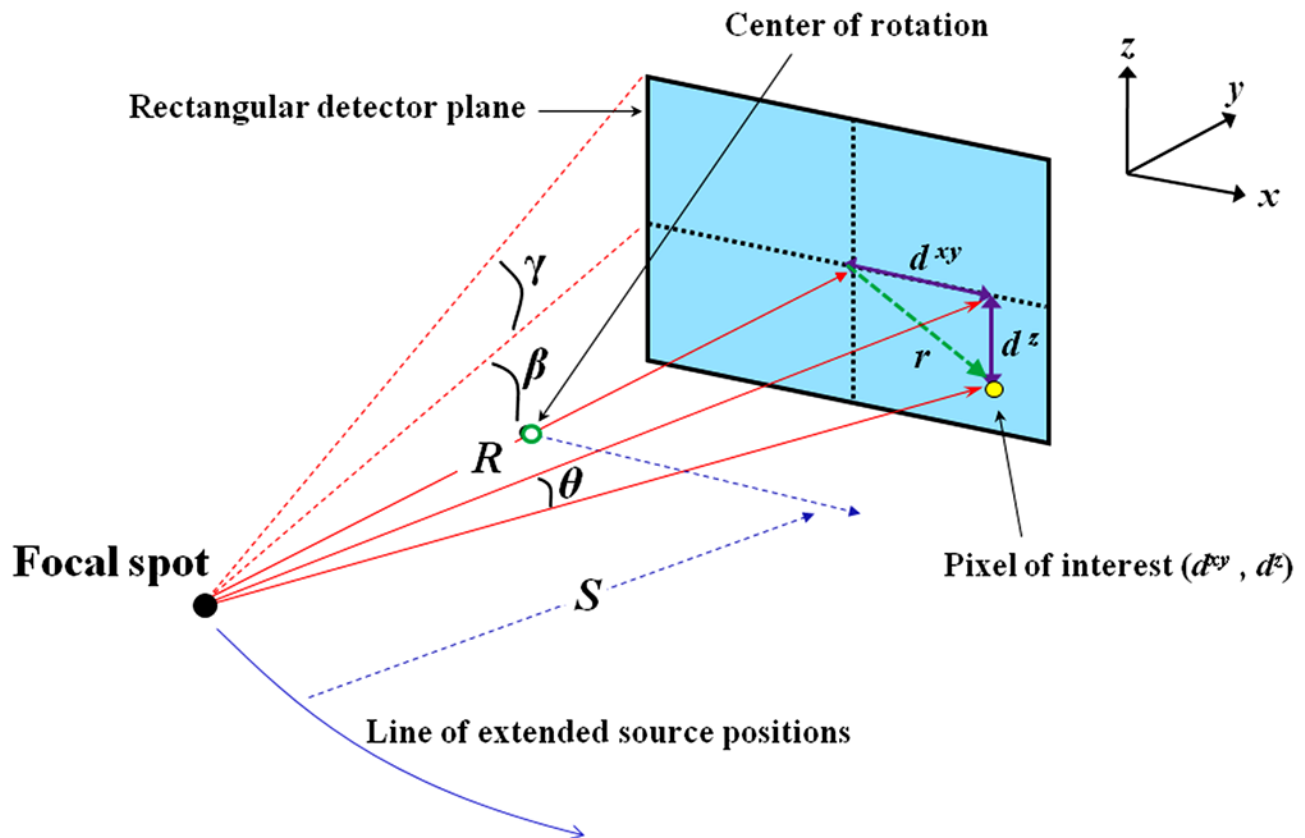

Fig. (1). Schematic view of the projection geometry for a rectangular detector plane the corresponding extended source. The geometric relations necessary for the calculation of the projection angle weighted theory can be derived.
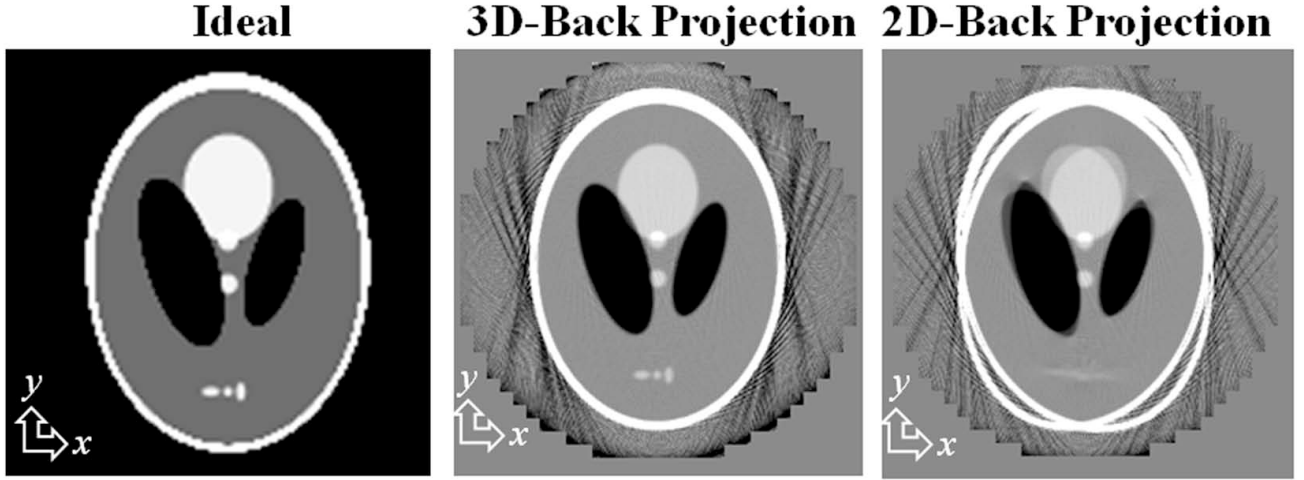
Ideal   3D-Back Projection   2D-Back Projection

Fig. (2). Comparison of 3D-FBP algorithm reconstruction images with images obtained from 3D-FBP reconstruction, 2-D FBP reconstruction of the different slice plane.

could reproduce the 3D information from the phantom. From these results, it appears necessary to use the 3D FBP method in reconstruction using cone-beam CT.

For a given 2D detector, the cone beam produced by the source illuminating a focus-detector can be described as follows. Let $\vec{R}$ be the vector from the center of the detector of the scanning system to the source and $\vec{D}$ the vector from the center of rotation to the center of the detector. For a scanning system moving along a circular trajectory, the positions of the source and detector result in

$$\vec{R} = R \begin{pmatrix} \cos\alpha \\ \sin\alpha \\ 0 \end{pmatrix} \qquad \vec{D} = \begin{pmatrix} -\cos\alpha \\ -\sin\alpha \\ 0 \end{pmatrix} \qquad (1)$$

The set of 2D projection data $p^f(\alpha, \beta, \gamma)$ on a focus-detector measured along a circular focus-detector trajectory is parameterized by the angular focus position on the circular trajectory $\alpha \in [0, 2\pi]$, the fan angle $\beta \in [-\beta_{max}, +\beta_{max}]$, and the cone angle $\gamma \in [-\gamma_{max}, +\gamma_{max}]$. To obtain the projection data in a rectangular detector plane for use in 3D cone-beam reconstruction, resampling to Cartesian coordinates in the column direction is applied. The projection data on the resulting rectangular detector are parameterized in the following by $p^{uv}(\alpha, d^{xy}, d^z)$, with $(\cos\alpha, \sin\alpha, 0)$ being the vector normal to the rectangular plane. d^{xy} and d^z are the two Cartesian coordinates within the new rectangular detector plane, where $d^z(d^{xy})$ marks the direction in the detector plane orthogonal to the plane of rotation:

$$p^f(\alpha, \beta, \gamma) \rightarrow p^{uv}(\alpha, d^{xy}, d^z) \qquad (2)$$

The two Cartesian coordinates have a range of $d^{xy} \in [-d^{xy}_{max}, +d^{xy}_{max}]$ and $d^z \in [-d^z_{max}, +d^z_{max}]$. The maximum values are calculated as follows:

$$d^{xy}_{max} = R \tan(\beta_{max}) \qquad (3)$$

and

$$d^z_{max} = R \tan(\gamma_{max}). \qquad (4)$$

This rectangular plane is the largest that fits completely into the convex area. The data contained in the outer area do not need to be measured in the original focus-detector plane if the proposed method is used. Therefore, the use of a suitable collimator reduces the dose applied to the patient or object.

Consequently, a simplified 3D FBP method can be applied to the rebinned data lacking the distance weighting factor $\left(\dfrac{R}{r}\right)^2$, which is well known from the Feldkamp algorithm approach. While R is the length of the vector R from the source to the center of the detector of rotation, r describes the length of the vector from the source to a voxel under consideration projected onto $\vec{R}$ within the original method. Thus, the resulting Feldkamp algorithm has reduced computational complexity and can be expressed in the following manner:

$$(\text{Step 1}) \quad g_1 = p^f(\alpha, \beta, \gamma) \cdot \omega(\beta, \gamma) \qquad (5)$$

$$(\text{Step 2}) \quad g_2 = g_1(\alpha, \beta, \gamma) * h(\beta) \qquad (6)$$

$$(\text{Step 3}) \quad f\!\left(\vec{x}\right) = \frac{1}{2\pi} \int_0^{2\pi} \left(\frac{R}{r}\right)^2 g_2(\alpha, \beta, \gamma) \, d\alpha \qquad (7)$$

where equation (5) and (6) is pre processing, equation (7) is the reconstruction image from the 2D projection data. The pre-weighting factor $\omega(\beta, \gamma)$ is geometrically interpreted as the angle between the ray and the central ray of the projection. The one-dimensional ramp filter $h(\beta)$ is applied along the lines to the plane-of-rotation in the detector plane (d^{xy} direction).

3.1.2. Evaluation Study

We performed computer simulation using a 3D Shepp-Logan phantom and a 3D disk phantom to evaluate the Feldkamp algorithm. The source-to-origin distance was set to 4.0. The number of detectors per cone-beam projection was 256×256 (rectangular plane). The size of the 2D detector plane was 2.0×2.0. (Full cone angle at 28.01 degree, fan angle at 28.01 degree). The number of projections was 360. The numbers of radial and angular samples were 256 and 360, respectively. Each reconstructed image volume had dimensions of $2.0 \times 2.0 \times 2.0$ and contained $256 \times 256 \times 256$ voxels.

In the numerical simulation, the traditional Feldkamp algorithm reconstruction suffered from significant decrease of intensity from the mid-plane, which is a well-known drawback (Figs. **3-5**).

The resolution properties of the cone-beam CT system (DynaCT, Siemens AG Co., Germany) were evaluated by measuring the modulation transfer function (MTF). To obtain the inherent resolution property in the cone-beam CT system, the MTF was obtained by 2D Fourier transformation of the images. In the reconstruction of cone-beam CT images (512×512 matrix, 0.1 mm/pixel), MTF was obtained by fast Fourier transformation of the line spread function. Representative MTF results are presented in Fig. (**6**). From this figure, it can be seen that the traditional Feldkamp algorithm reconstruction suffered from significant reduction of the MTF value away from the mid-plane, which is a well-known drawback of the Feldkamp algorithm. On the other hand, the Feldkamp algorithm reconstructs better near the central plane than away from the central plane.

The cone-beam artifact has a large cone angle and becomes greater at greater distances in the longitudinal direction (Fig. **7**). In addition, it was confirmed that when there are large amounts of artifacts, the trajectory of the projected data is larger. Figure **8** represents the use of the Feldkamp algorithm on human full-scan data at different cone angles obtained using cone-beam CT. The Feldkamp algorithm was found to be effective because the cone-beam artifacts were reduced under basal conditions when the cone angle was large.

The effect of scatter from a 3D object which is incident on two dimensions of a detector with a large field cannot be ignored. We confirmed that a capping phenomenon that decreases the pixel value of a rearranged image results when the scatter of the content increases in the center of the subject. We used a bow-tie filter [30,31] to correct this capping and could suppress the capping for intensity distribution so that direct X-ray intensity after subject transmission becomes same (Fig. **9**). When a pixel value of a
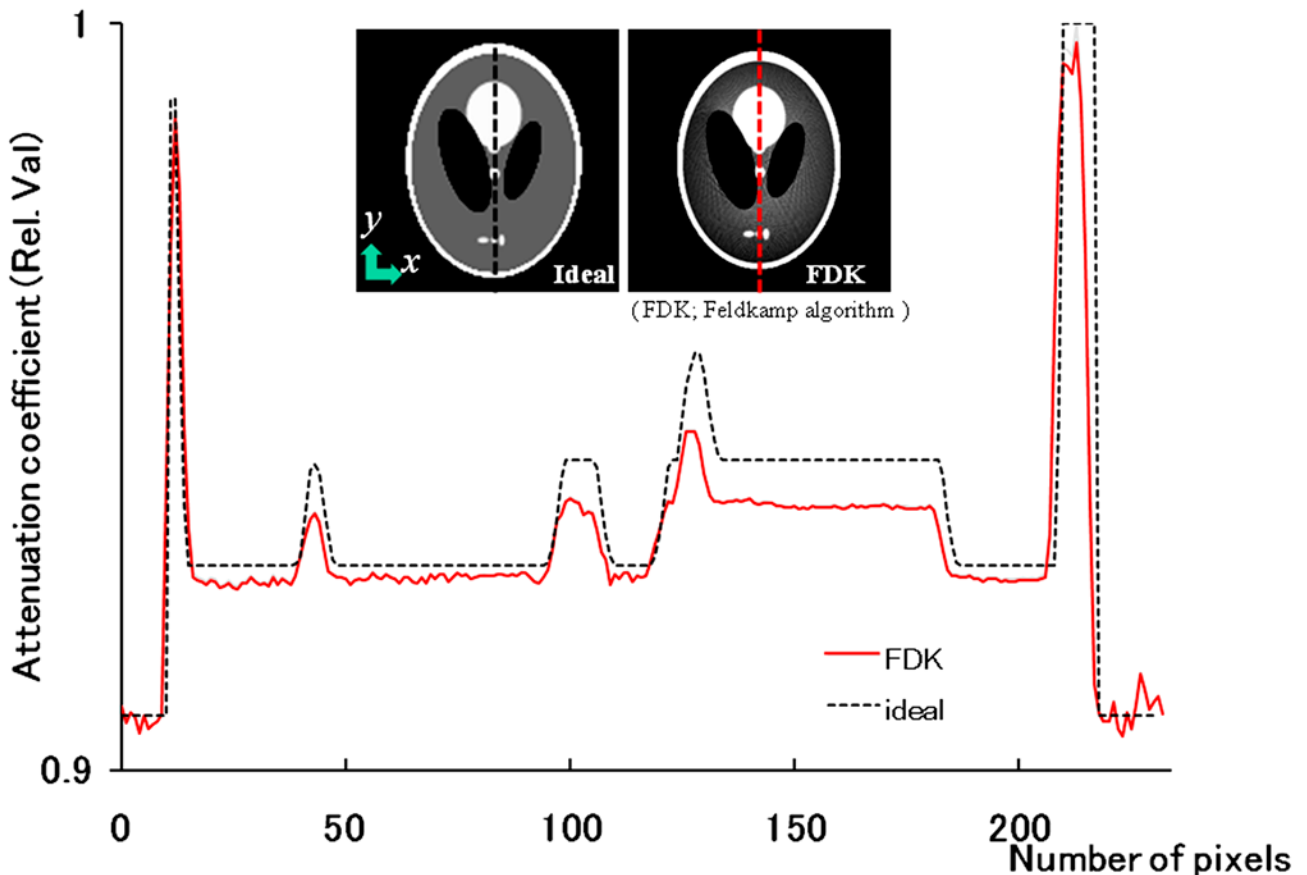

Fig. (3). Intensity profiles (The central vertical line in the selected slice of the 3D Shepp-Logan phantom). Ideal and reconstructed slices of the 3D Shepp-Logan phantom at z=-0.25 with Feldkamp reconstruction method.
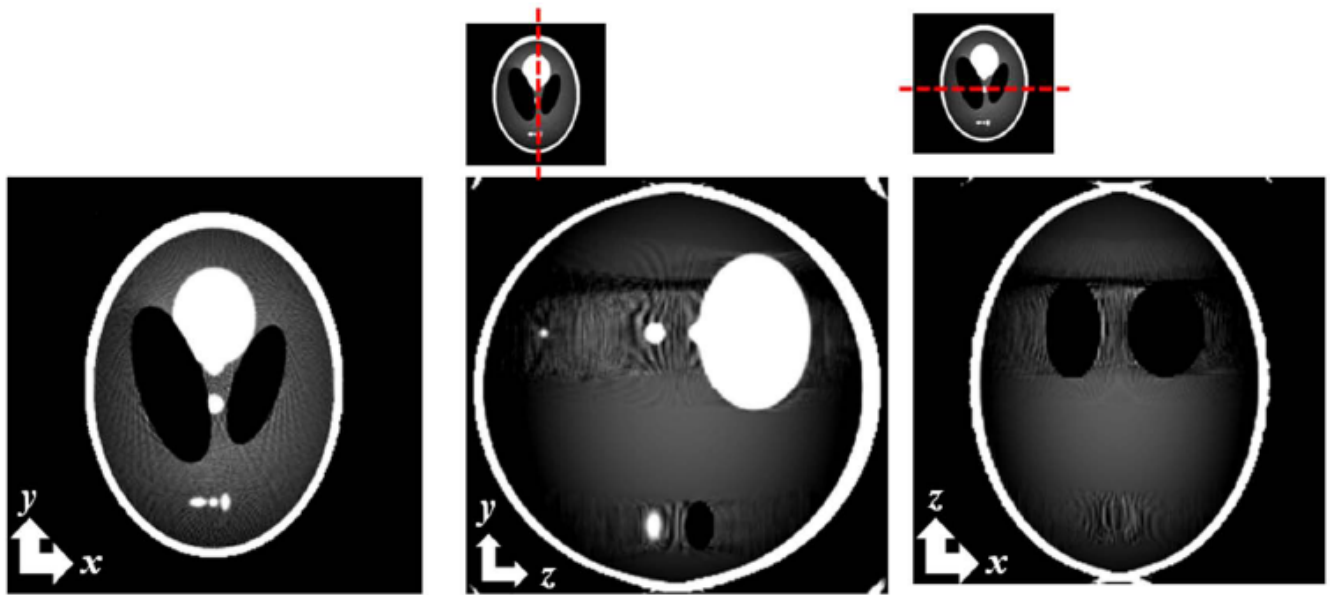
Fig. (4). Reconstructed slices of the 3D Shepp-Logan phantom at different plane with Feldkamp reconstruction method.
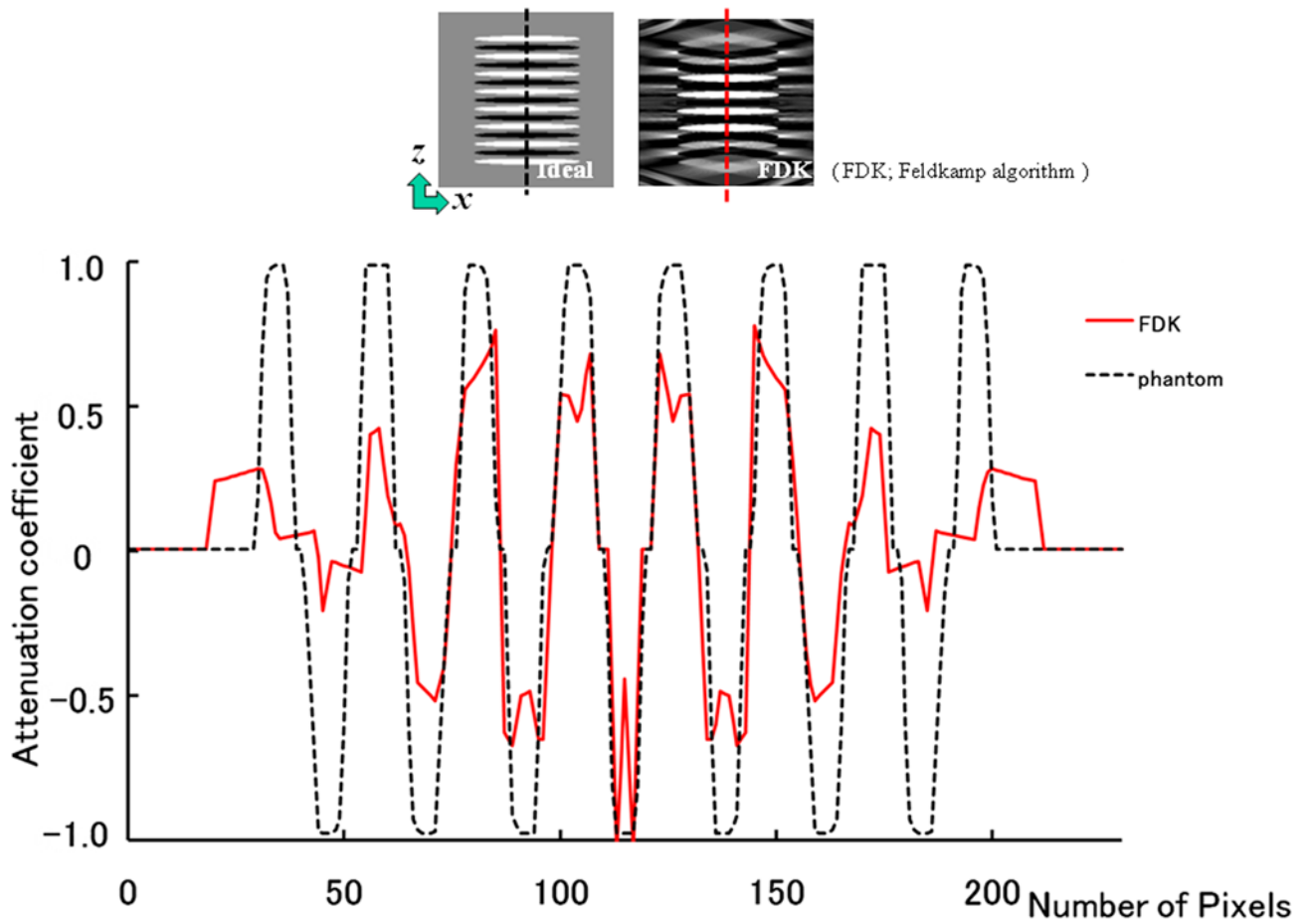

Fig. (5). Intensity profiles (The off-central vertical line in the selected slice of the 3D Disk phantom (corresponding profiles). Ideal and reconstructed slices of the 3D Disk phantom at y = 0.0 with Feldkamp algorithm image, respectively.

rearrangement image does not use a bow-tie filter, there is a tendency to decrease large in image edge regions, but can confirm what is improved when bow-tie filter is used (Fig. **10**).
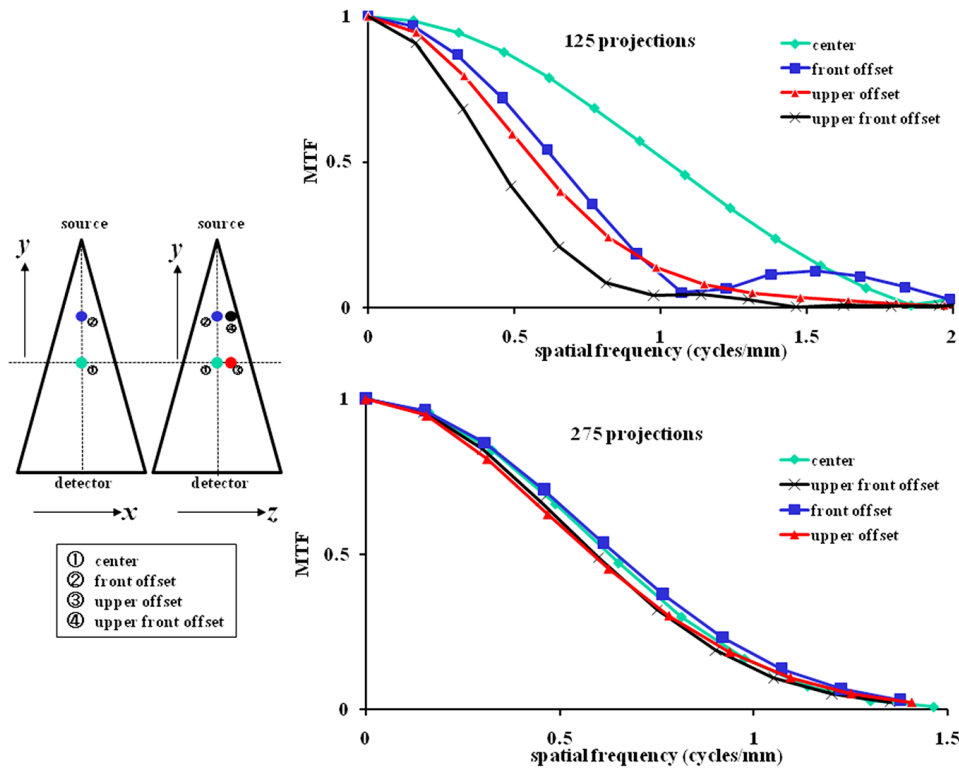
Fig. (6). A comparison of resolution in the mid-plane vs. off-center plane for the cone-beam CT system (in various positions in the scanner field of view (FOV), for two different numbers of angular projections). The shape of the phantom was used microspheres object (Pb , 0.3mmφ). The MTF calculated line spread function (LSF) by analyzing fast Fourier transform (FFT).
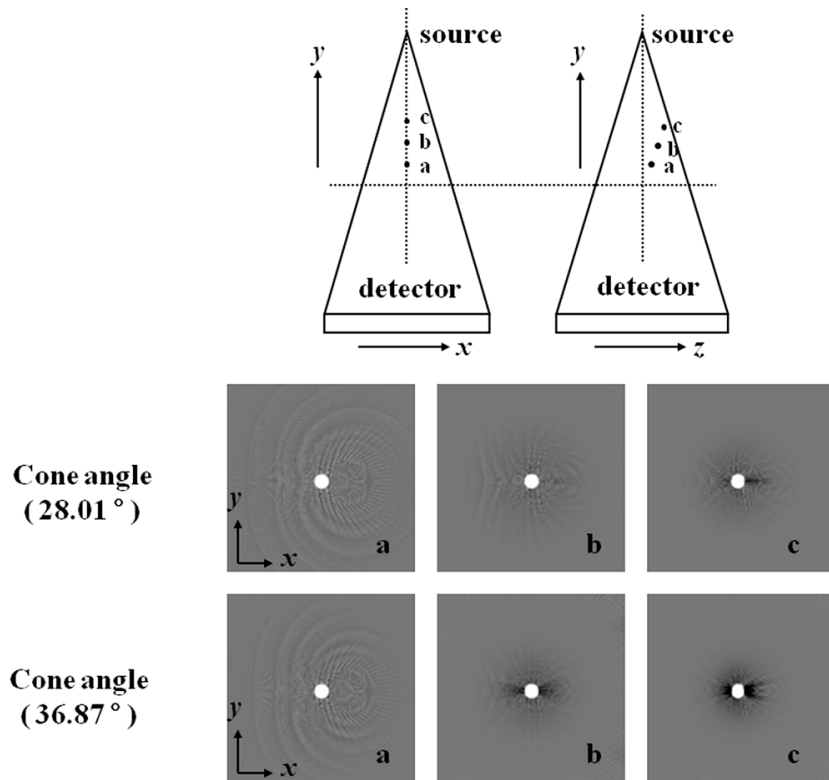

Fig. (7). Comparison of 3D-FBP algorithm (Feldkamp algorithm) reconstruction images with images obtained from con-angle at 28.01 degree, cone-angle at 36.87 degree of the different microsphere phantom position. The cone-beam artifact of a reconstruction image tends to become large cone-angle and away from the mid-plane.
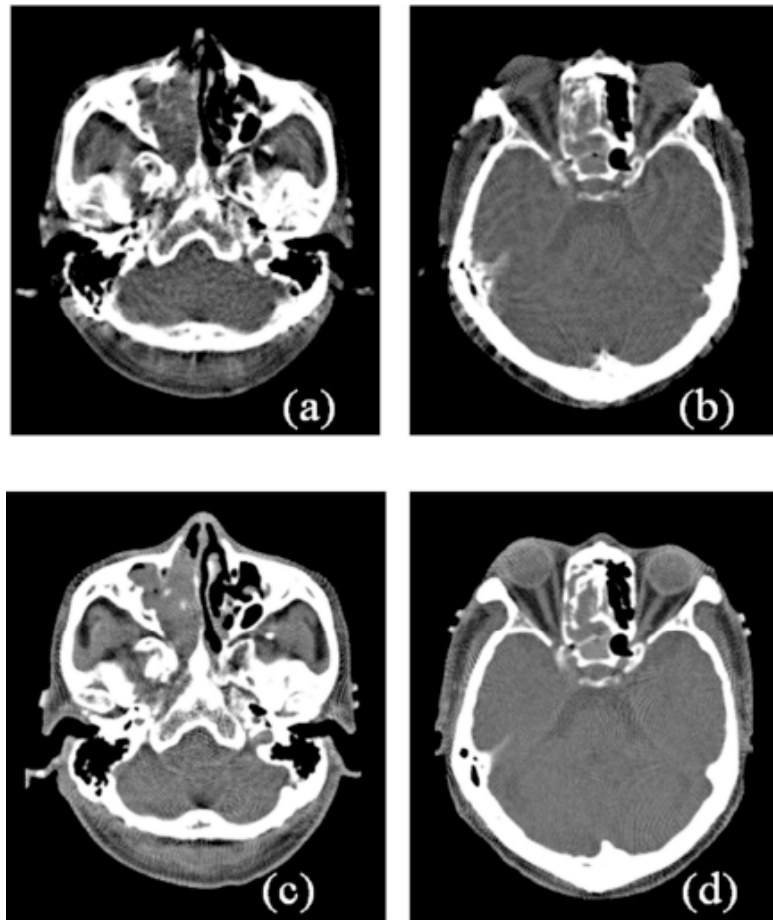
Fig. (8). Real and different reconstruction slices of the human head origin (a 60-year-old man, night nasal tumor) at trans-axial direction with Feldkamp reconstruction algorithm. (**a**) and (**b**): cone-angle at 28 degree. (**c**) and (**d**): cone-angle at 37 degree.
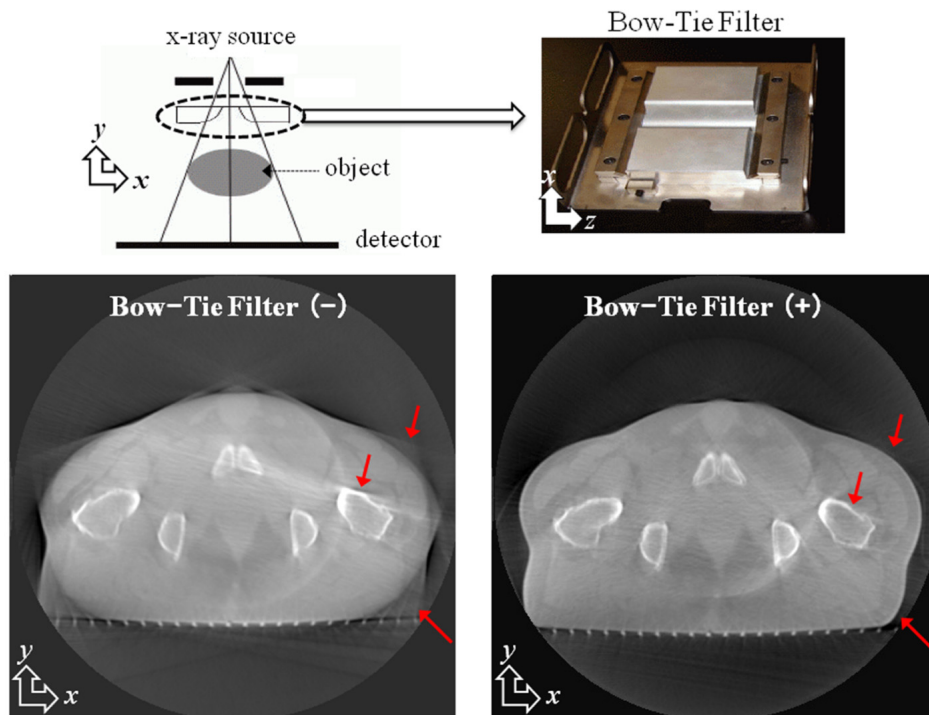

Fig. (9). Real and slices of the human pelvis (prostate) at axial direction with bow-tie filtering and non bow-tie filtering processing, respectively.
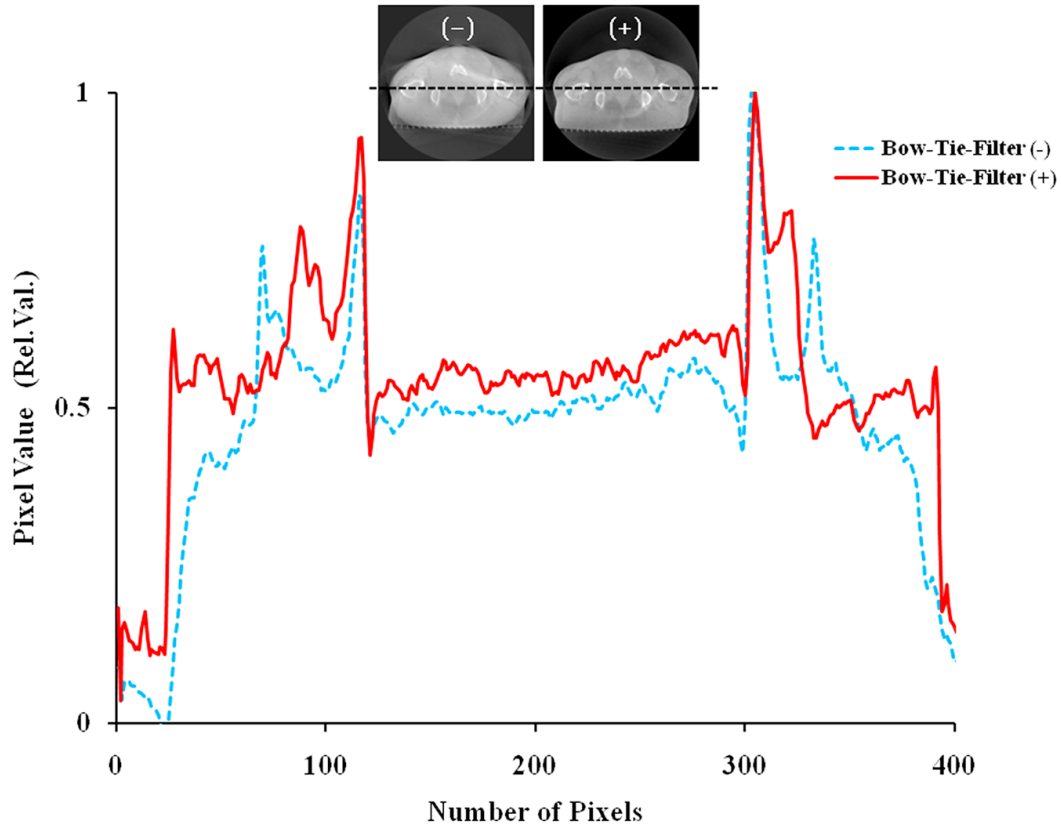
Fig. (10). Intensity profiles (The central horizontal line in the selected slice of the human pelvic image).

3.2. Tomosynthesis System

3.2.1. Reconstruction Algorithm

A modified FBP algorithm has been reported that provides a description of filtering that can be used in combination with backprojection to yield tomosynthesis slice images with desired properties [32,36]. The following description of the generalized 3D impulse function is adapted from a previous study [33]. The 3D version of the Fourier slice theorem states that when a 2D image of an object is acquired at some particular orientation to that object, the 2D Fourier transform of that projection image yields a plane through the 3D Fourier space of the object. Characteristics are estimated in modified FBP by low-pass filter processing. The Fourier space low-pass filtering unit applies a low-pass filter in the direction along the sectional axis of Fourier space data that have undergone a 3D Fourier transform (Fig. **11**). This process is effective in reducing artifacts in the 3D volume data generated by a 3D back Fourier transform of the Fourier space data after low-pass filtering. The 3D Fourier transform of the 3D volume data generated by backprojection is based on the following equation (8):

$$F(\omega_x, \omega_y, \omega_z) = \iiint f(x,y,z) \cdot \exp\left\{-j(\omega_x \cdot x + \omega_y \cdot y + \omega_z \cdot z)\right\} dx \cdot dy \cdot dz \quad (8)$$

where $f(x,y,z)$ is the simple backprojection intermediate image, and x, y, and z are real numbers. The meaning of the filtering process performed in 3D Fourier space is described below, and is mathematically expressed by the following equation (9):

$$FM(\omega_x, \omega_y, \omega_z) = F(\omega_x, \omega_y, \omega_z) \cdot M(\omega_x, \omega_y, \omega_z) \quad (9)$$

where $FM(\omega_x, \omega_y, \omega_z)$ is the filtered 3D Fourier distribution image, and $M(\omega_x, \omega_y, \omega_z)$ is a function representing filter characteristics. The filtering process done in 3D Fourier space is to weight the 3D Fourier distribution image of complex data, with the real-valued filter function M dependent on the respective frequency values. The weighting function M is compressed in the ω_z-direction. $M(\omega_x, \omega_y, \omega_z)$ is expressed by the following equation (10) as a product of three functions representing the filter characteristic:

$$M(\omega_x, \omega_y, \omega_z) = H_{prof}(\omega_z) \cdot H_{spec}(\omega_r) \cdot H_{inverse}(\omega R) \quad (10)$$

A typical example of each filter function system shown in equation (10) is described next. $H_{prof}(\omega_z)$ has a low-pass filter characteristic, i.e., a Gaussian characteristic, which is expressed by the following equation (11):

$$H_{prof}(\omega_z) = \exp\left(-0.693\left[\frac{\omega_z}{CFD}\right]^2\right) \quad (11)$$

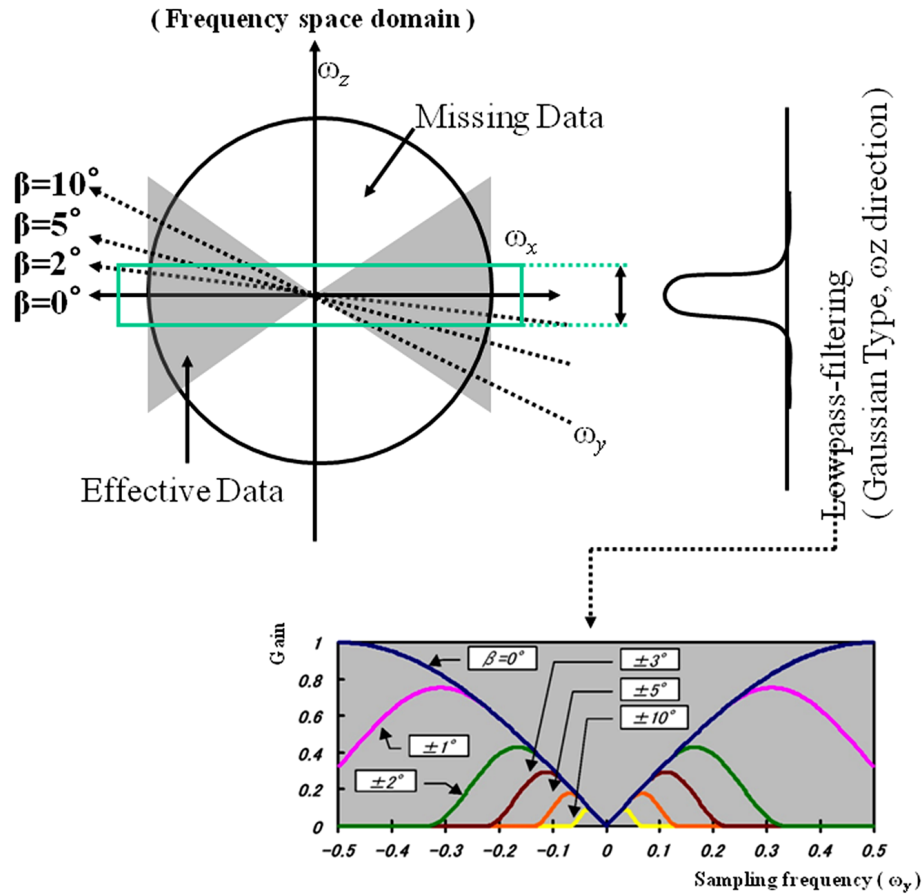where CFD is the frequency with the Gaussian attenuation halved.

Fig. (11). Illustration of the effective area and defect area in tomosynthesis. The Fourier space data having undergone three-dimensional Fourier transform have missing cones centred on the ωz-axis, with the vertices, meeting at the origin of the Fourier space coordinates. Thus, Fourier space low-pass filtering is characterized by applying a low-pass filter in the direction of the sectional axis to lessen the influence of the missing cone data.

$H_{spec}(\omega_r)$ has a filter characteristic which is expressed by the following equation (12):

$$
\begin{bmatrix}
H_{spec}(\omega_r) = 1 & \left(case \quad \omega_r < \dfrac{CFR-WFR}{2}\right) \\
H_{spec}(\omega_r) = \dfrac{1-\sin(\omega_r - CFR)\cdot \pi / WFR}{2} & \left(case \quad \dfrac{CFR-WFR}{2} < \omega_r < \dfrac{CFR+WFR}{2}\right). \\
H_{spec}(\omega_r) = 0 & \left(case \quad \dfrac{CFR+WFR}{2} < \omega_r\right)
\end{bmatrix}
\quad (12)
$$

However, $\omega_r = \sqrt{\omega_x{}^2 + \omega_y{}^2 + \omega_z{}^2}$. The function has a sine wave form with high-frequency components smoothly attenuated. CFR is the cut-off frequency, and WFR is the total transition frequency width of the filter strength. $\dfrac{CFR+WFR}{2}$ is the Nyquist frequency and $\dfrac{CFR-WFR}{2}$ is the no processing region frequency. This $H_{spec}(\omega_r)$ removes high frequency components from the origin of the 3D Fourier space. $H_{inverse}(\omega R)$ has the filter characteristic which is expressed by the following equation (13):

$$
H_{inverse}(\omega_R) = |\omega_R| \quad , \quad \omega_R = \sqrt{\omega_x{}^2 + \omega_y{}^2}
\quad (13)
$$

The 3D back Fourier transforms the Fourier space data back to 3D volume data, having undergone Fourier space low-pass filtering. The 3D back Fourier transform is expressed by the following equation (14):

$$
fm(x,y,z) = \frac{1}{8}\pi^3 \iiint FM(\omega_x,\omega_y,\omega_z)\cdot \exp\left\{j(\omega_x\, x + \omega_y\, y + \omega_z\, z)\right\} d\omega_x d\omega_y d\omega_z
\quad (14)
$$

Equation (14) is the transformation from the frequency domain to the space domain. It is the inverse of the relationship described by equation (8).

3.2.2. Evaluation Study

The plane locations were center plane (0 mm) and off-center plane from the object location. The off-center plane is located 70 mm from the center plane. The image reconstructed at the center plane shows that the object is faithfully reconstructed on the focal plane. In the numerical simulation, the 3D Shepp-Logan phantom was used for evaluation by comparing the modified FBP algorithm with the Feldkamp-type algorithm. Representative results of reconstruction are presented in Fig. (**12**). The traditional Feldkamp-type reconstruction suffered from significant decrease of intensity from the mid-plane (Fig. **12** on "off-center"), which is a well-known drawback of the Feldkamp-type algorithm. On the other hand, our modified FBP
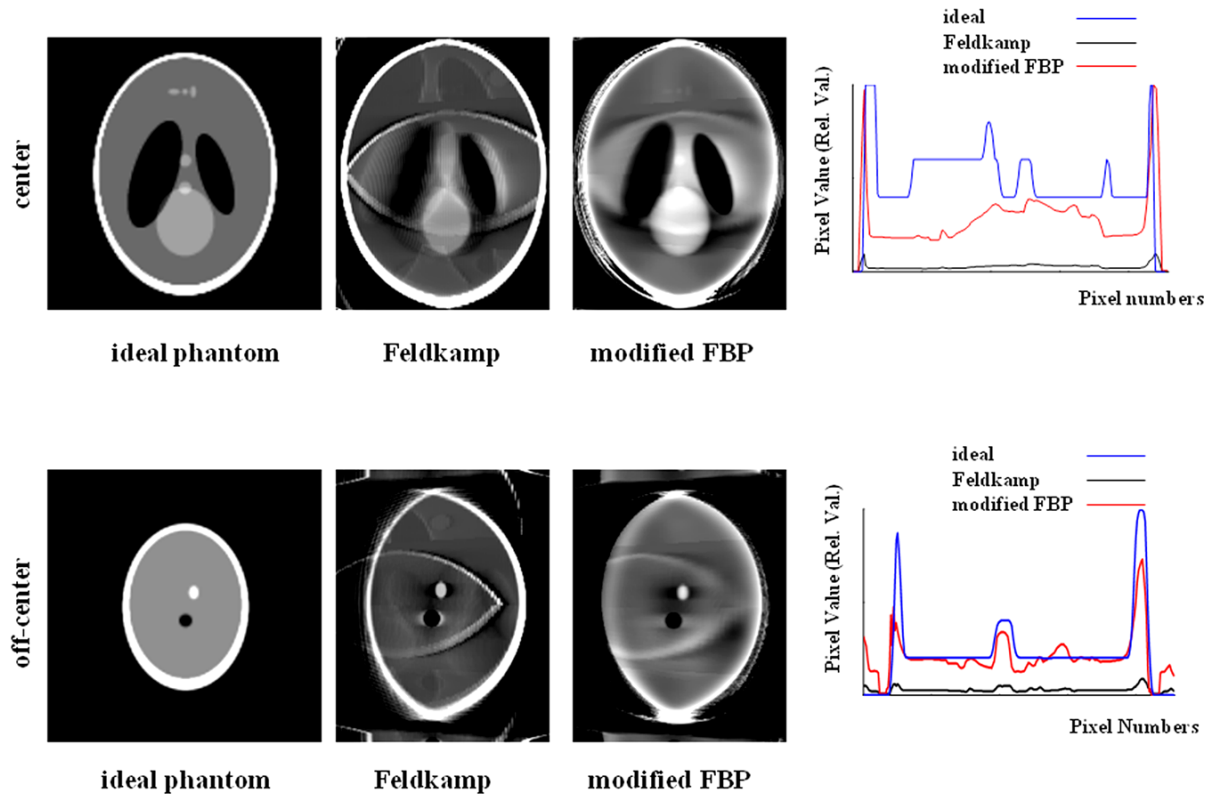
Fig. (12). Reconstruction simulation images of the three-dimensional Shepp-Logan phantom at different heights. In addition, comparison of axial profile plots through the reconstructed 3D image function in comparison with discretization of the 3D Shepp-Logan phantom. A data set with 90 projection images and a tomographic angle of 40°was obtained.

algorithm improved the image quality remarkably, and yielded better image quality (both center and off-center plane) than the Feldkamp-type algorithm.

On the digital linear tomosynthesis images, the temporomandibular joint was present outside the reconstruction plane and was blurred, as shown in Fig. (**13**). Panoramic radiography did not demonstrate an intracapsular fracture. Using panoramic radiography, it is not difficult to detect inflammatory conditions (Fig. **13a**). Conventional tomography largely eliminates the problem of superposition of anatomical structures encountered in plain films and panoramic radiographs, allowing all mineralized aspects of the joint to be evaluated. Inflammatory evaluation is better than conventional radiography. A major disadvantage of conventional tomography is the lack of visualization of the soft tissues of the joint, which is a problem in evaluating disk position (Fig. **13b**, **c**). The use of digital linear tomosynthesis improved the visualization of the underlying tissue detail by deblurring the overlying structures. This allowed better visualization of the tissue detail directly below the temporomandibular joint structures (Fig. **13d**).

The results of the real study were compared with those using the radiograhy image (direct flat panel detector (FPD), amorphus selenuim type) and tomosyntheis image. The tomosyntheis image is superior to the conventional radiography image in the detection of simulated pulmonary nodules (Fig. **14**).

4. FUTURE DIRECTIONS

In the reconstruction of cone-beam CT, when a wide imaging range is required, FBP processing that takes account of the cone angle is needed. This reproduces subject information as faithfully as possible, and ideally, 3D FBP processing should be used in such a manner as to prevent deterioration of image artifacts. One of the image quality improvement problems of cone-beam CT is to develop a reconstruction method to reduce the cone-beam artifact. Another problem in image quality improvement is the effect of x-ray scatter. In the trial that used bow-tie filter, image processing disappeared. According to the manufacturer, owing to the use of the cone-shaped X-ray beam and the "smart beam technology," the absorbed dose from a cone-beam CT scan is approximately equivalent to two to five panoramic exposures; however, this claim needs further investigation.

Clinical reports have indicated the usefulness of cone-beam CT in an angiography system and image-guided radiation therapy in a current medical service system [34, 35]. However, cone-beam artifact and scatter measures are problems affecting the image quality of the reconstruction image. Many researchers suggest that computer simulation methods may improve control over the cone-beam artifact. Other reports indicate that it can reduce scatter X-ray measure by bow-tie filtering and image processing.
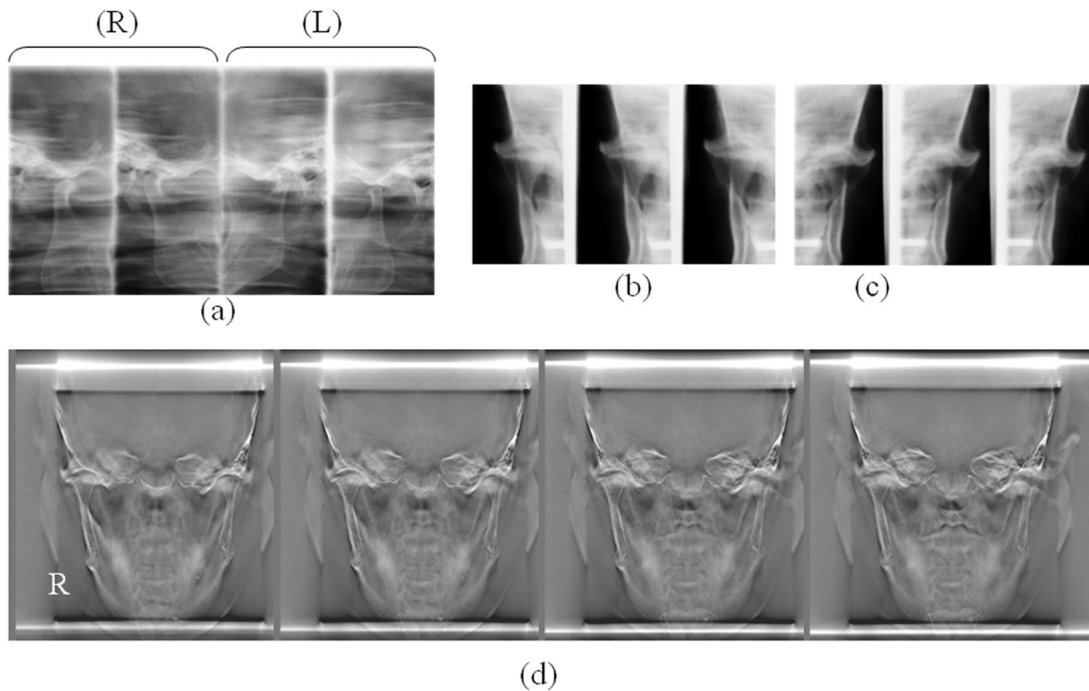
Fig. (13). Case report: 56-year-old woman; inflammatory disorder of the right temporomandibular joint. (**a**): Panoramic radiograph (closed and open mouth) showing the mandibular condyle. (**b**): Conventional tomography showing the right mandibular condyle. (**c**): Conventional tomography showing the left mandibular condyle. (**d**): X-ray digital linear tomosynthesis images (different level positions) showing the mandibular condyle. A data set with 90 projection images and a tomographic angle of 40°was obtained.
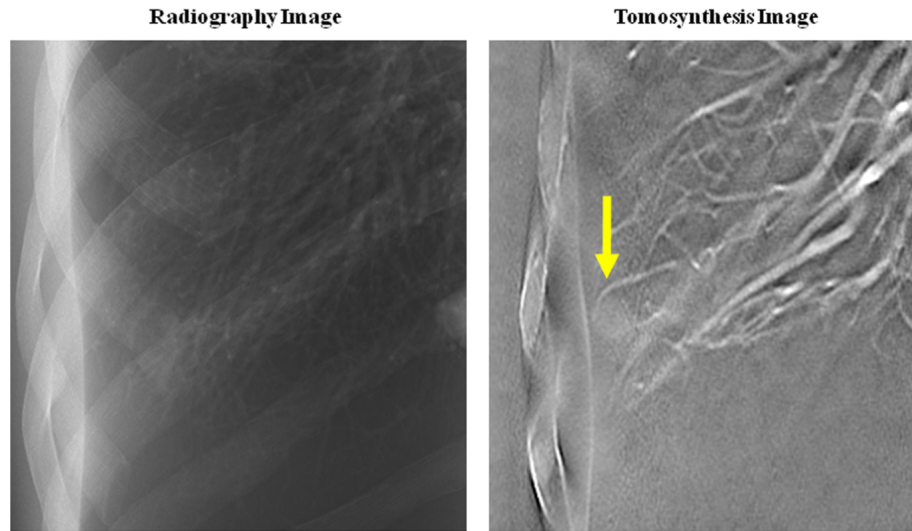

Fig. (14). Real and reconstructed slices of the chest phantom at coronal direction with radiography image and tomosynthesis image. A data set with 90 projection images and a tomographic angle of 40°was obtained. (simulated pulmonary nodule; Hounsfiled Unit at -600, 7mmφ, grand glass opacity type).

The digital linear tomosynthesis system used here shows adequate overall performance, but it is obvious that its effectiveness is strongly dependent on scanning parameters (tomographic angle, number of views, and section thickness). Digital linear tomosynthesis imaging provides a general overview of the temporomandibular joint and chest pahntom, which is sometimes valuable in cases with severe morphological abnormalities. Therefore, this method may be considered as the imaging technique of choice for the investigation of bony changes and soft tissue (such as pulmonary nodules).

5. CONCLUSIONS

This paper provides a tutorial overview on volumetric reconstruction of cone-beam CT and digital tomosynthesis. It mainly focuses on introducing a Feldkamp algorithm and a digital linear tomosynthesis algorithm (modified FBP). Some results from simulations and real measurements are presented in order to give an explanation of the various

pitfalls of the most used reconstruction techniques. We expect that in future it will be possible to detect diseases at an early stage using cone-beam geometry devices that provide high image quality with low exposure dose.

REFERENCE

[1]   Grangeat P, Sire P, Guillemaud R, La V. Computational imaging and vision: three-dimensional image reconstruction in radiology and nuclear medicine. Kluwer Academic Publishers, Dordrecht: USA 1996.

[2]   Grangeat P, Sire P, Guillemaud R, La V. Contemporary perspectives in three-dimensional biomedical imaging: indirect cone-beam three-dimensional image reconstruction. IOS Press: The Netherlands 1997.

[3]   PMB. 1997 International meeting on fully three-dimensional image reconstruction in radiology and nuclear medicine. Phys Med Biol 1998; 43: 715-1048.

[4]   Carlsson CA. Imaging modalities in x-ray computerized tomography and in selected volume tomography. Phys Med Biol 1999; 44: 23-56.

[5]   Sliver MD. High Helical pitch cone-beam computed tomography. Phys Med Biol 1998; 43: 847-856.

[6]   Tam KC, Samarasekera S, Sauer F. Exact cone-beam CT with a spiral scan. Phys Med Biol 1998; 43: 1015-1024.

[7]   Taguchi K, Aradate H. Algorithm for image reconstruction in multi-slice helical CT. Med Phys 1998; 25: 550-561.

[8]   Noo F, Defrise M, Clack R. Single-slice rebinning method for helical cone-beam CT. Phys Med Biol 1999; 44: 561-570.

[9]   Kudo H, Noo F. Cone-beam filtered backprojection algorithm for truncated helical data. Phys Med Biol 1998; 43: 2885-2909.

[10]   Feldkamp LA, Davis LC, Kress JW. Practical cone-beam algorithm. J Opt Soc Am A 1984; 1: 612-619.

[11]   Tuy HK. An inversion formula for cone-beam reconstruction. SIAM J Appl Math 1983; 43: 546-552.

[12]   Smith BD. Image reconstruction from cone-beam projections: necessary and sufficient conditions and reconstruction methods. IEEE Trans Med Imaging 1985; 4: 14-25.

[13]   Grass M, Kohler TH, Proksa R. 3D cone-beam CT reconstruction for circular trajectory. Phys Med Biol 2000; 45; 329-347.

[14]   Turbell H. Cone-beam reconstruction using filtered backprojection. Linkoping Studies in Science and Technology. 2001; Thesis no 672.

[15]   Noo F, Kudo H, Defrise M. Approximate Short-scan Filtered backprojection for Helical CB reconstruction. IEEE Nuclear Sci Symp 1998; 3: 2073-2077.

[16]   Flohr T. Clinical benefits of a multi row detector spiral CT system. Radiology 1997; 205: 214-215.

[17]   Wang G, Vannier MW. Pitch analysis in multi-slice spiral/helical CT. Med Phys 1999; 26: 2648-2653.

[18]   Mori S, Endo M, Komatsu S, *et al.* A combination-weighted Feldkamp-based reconstruction algorithm for cone-beam CT. Phys Med Biol 2006; 51(16): 3953-3965.

[19]   Mori S, Endo M, Tsunoo T, *et al.* Physical performance evaluation of a 256-slice CT-scanner for four-dimensional imaging. Med Phys 2004; 31(6): 1348-1356.

[20]   Gomi T, Koshida K, Miyati T. Development of a non-linear weighted hybrid cone-beam CT reconstruction for circular trajectories. Comput Med Imaging Graph 2007; 31(7): 561-569.

[21]   Ziedses des Plante BG. Eine neue methode zur differenzierung in der roentgenographie (planigraphie). Acta Radiol 1932; 13: 182-192.

[22]   Grant DG. Tomosynthesis. A three-dimensional radiographic imaging technique. IEEE Trans Biomed 1972; 19: 20-28.

[23]   Stiel G, Stiel LG, Klotz E, Nienaber CA. Digital flashing tomosynthesis: A promising technique for angiographic screening. IEEE Trans Med Imaging 1993; 12: 314-21.

[24]   Warp RJ, Godfrey DG, Dobbins JT. Applications of matrix inverse tomosynthesis. Proc SPIE 2000; 3977: 376-383.

[25]   Duryea J, Dobbins JT, Lynch JA. Digital tomosynthesis of hand joints for arthritis assessment. Med Phys 2003; 30: 325-333.

[26]   Sone S, Kasuga T, Sakai F, *et al.* Image processing in the digital tomosynthesis for pulmonary imaging. Eur Radiol 1995; 5: 96-101.

[27]   Badea C, Kolitsi Z, Pallikarakis N. A 3D imaging system for dental imaging based on digital tomosynthesis and cone beam CT. Proc Int Federation Med Biol Eng 2001; 2: 739-741.

[28]   Niklason LT, Christian BT, Niklason LE, *et al.* Digital tomosynthesis in breast imaging. Radiology 1997; 205: 399-406.

[29]   Dobbins 3rd JT, Godfrey DJ. Digital x-ray tomosynthesis: curent state of the art and clinical potential. Phy Med Biol 2003; 48: R65-106.

[30]   Letourneau D, Wong JW, Oldham M, *et al.* Cone-beam-CT guided radiation therapy: technical implementation. Radiother Oncol 2005; 75(3); 279-286.

[31]   Nakagawa K, Yamashita H, Shiraishi K, *et al.* Verification of in-treatment tumor position using kilovoltage cone-beam computed tomography: a preliminary syudy. Int J Radiat Oncol Biol Phys 2007; 69(4): 970-973.

[32]   Gomi T, Hirano H. Clinical potential of digital linear tomosynthesis imaging of total joint artroplasty. J Digit Imaging 2008; 21(3): 312-22.

[33]   Lauritsch G, Harer WH. A theoretical framework for filtered backprojection in tomosynthesis. Proc SPIE 1998; 3338: 1127-1137.

[34]   Linsenmaier U, Rock C, Euler E, *et al.* Three-dimensional CT with a modified C-arm image intensifier: feasibility. Radiology 2002; 224(1): 286-292.

[35]   Letourneau D, Wong JW, Oldham M, *et al.* Cone-beam-CT guided radiation therapy: technical implementation. Radiother Oncol 2005; 75(3); 279-286.

[36]   Oikawa, S.: US20026463116B1 (**2002**).

[37]   Yang, H., Li Meihua, Koizumi, K., Kido, H.: JP06A0454664 (**2008**).

[38]   Shechter, G.: US20067020236 (**2006**).